Dylan Agius, Mladenko Kajtaz, Kyriakos I. Kourousis, Chris Wallbrink, Chun H. Wang, Weiping Hu, Jose Silva, Sensitivity and optimisation of the Chaboche plasticity model parameters in strain-life fatigue predictions, Materials and Design, Volume 118, 15 March 2017, Pages 107–121 (author accepted version)

Sensitivity and Optimisation of the Chaboche Plasticity Model Parameters in Strain-Life Fatigue Predictions

Dylan Agius[1], Mladenko Kajtaz[1], Kyriakos I. Kourousis[2,1 *], Chris Wallbrink[3], Chun H. Wang[4], Weiping Hu[3], Jose Silva[1]

[1]School of Engineering, RMIT University, Melbourne, Victoria, Australia.

[2]School of Engineering, University of Limerick, Limerick, Ireland.

[3]Defence Science and Technology Group, Fisherman's Bend, Melbourne, Victoria, Australia.

[4]School of Mechanical and Manufacturing Engineering, University of New South Wales, Sydney, New South Wales, Australia.

***Corresponding Author:** kyriakos.kourousis@ul.ie

Abstract

The aerospace industry is widely employing strain-life methodologies for structural fatigue predictions. Under spectrum loading, overloads significantly affect the fatigue, therefore it is very important to accurately account for the cyclic transient deformation phenomena. Describing these phenomena requires advanced plasticity models that involve a set of material parameters. Even for the well-known Chaboche model, there is lack of understanding of each parameter's sensitivity

in strain-life fatigue calculation among engineering practitioners. A parameter optimisation technique using a multi-objective genetic algorithm is applied for the Chaboche model parameters by employing varying strain and stress controlled uniaxial data from tests on Aluminium Alloy 7075-T6. The parameters obtained from each of the optimisations and for various workflows, are then used in strain-life fatigue calculations with a Defence Science and Technology Group in-house software. Fatigue life predictions for P-3C aircraft load spectra are compared against experimental lives obtained from the Masing model to ascertain the parameters offering the most accurate results. The optimum uniaxial material dataset for strain-life predictions employing the Chaboche model is determined. The results of this study offer new insights of the model parameters' function and their sensitivity in fatigue predictions.

Keywords: cyclic plasticity; fatigue; Chaboche model; optimisation; aluminium alloys; aircraft structures.

1. Introduction

Cyclic transient effects such as strain ratcheting and mean stress relaxation can have an influence on the fatigue damage in a structure, particularly under low cycle fatigue. Consequently, it is important to account for these phenomena in fatigue life predictions. Strain-life approaches are an important fatigue life prediction methodology in the structural integrity management of aircraft. The most common material plasticity model applied in such methodologies is the Masing model [1]. In the Masing model, the elastoplastic hysteresis loops are constructed from a series of stabilised cyclic stress strain curves obtained from symmetrical strain controlled testing. The most significant drawback of the Masing model is its inability to recognise transient cyclic phenomena, such as strain ratcheting and mean stress relaxation, both having an influence on fatigue life [2-8].

Strain ratcheting, or else referred as cyclic creep (progressive accumulation of plastic strain under cycling), is a phenomenon which occurs during asymmetric stress controlled loading, while mean stress relaxation occurs during asymmetric strain-controlled loading (stabilisation of hysteresis loop evolution after a number of cycles). However, for components with stress raising features (such as notches or cut-outs), a combination of the two phenomena may occur at the notch root [9], which highlights the importance of taking into consideration both phenomena when it comes to fatigue life predictions. This is particularly important in service life loading since load sequence effects can have a significant influence on the fatigue life [10].

Constitutive plasticity models capable of accurately simulating cyclic transient behaviour have been shown to improve fatigue predictions [3, 11-14] and the importance of their application to specifically strain-life fatigue is becoming more apparent [14, 15]. A difficulty associated with the implementation and wider usage of these cyclic plasticity models is in the identification of their parameters. As the models increase their level of sophistication and complexity, the number of material parameters has increased as well. This has led to the introduction of various material parameter optimisation techniques, in order to ease/streamline the identification process and improve the accuracy of the model predictions [16-27]. However, the sensitivity of the strain life fatigue predictions to the model parameters requires a thorough assessment, owing to the complexity of many real-life load spectra. This knowledge is important to the identification of the plasticity model parameters, obtained from uniaxial test data, which are able to provide the most accurate strain life fatigue predictions.

This paper presents a sensitivity analysis conducted to identify the optimal uniaxial dataset combinations that can be used to determine the parameters of a widely used cyclic plasticity model.

Both symmetric and asymmetric strain and stress controlled test data from Aluminium alloy (AA) 7075-T6 have been used for the calibration and implementation of the model in strain life fatigue prediction. In this analysis, a number of genetic algorithm (GA) optimisation strategies have been employed to evaluate the effectiveness of material parameters for various operating load spectra. Moreover, out of this process, those optimisation strategies achieving higher accuracy in fatigue calculation are identified.

2. Research Methodology

2.1 Mechanical Testing

2.1.1 Test Setup and Coupons

An extensive knowledge of the AA 7075-T6 response under cycling loading was required for the calculation of the model parameters. This involved the execution of symmetric and asymmetric strain-controlled, as well as asymmetric stress-controlled tests. The tests were performed on a MTS servo-hydraulic closed-loop testing machine with a capacity of 100kN, using 0.1 Hz sine waves. All strain measurements were made using a 10mm extensometer. All tests were conducted at room temperature (consistent with past DST Group research work on notched coupon tests and tests conducted to develop the strain-life curves [28, 29]).

The test coupons were machined from blanks cut from 12mm thick plate, with the long axis of the coupon parallel to the rolling direction. Typically, rolled/extruded aerospace aluminium alloys (such as AA 7075) are expected to exhibit some anisotropy in the longitudinal/transverse direction, mainly due to the existence of residual stresses arising from heat treatments and plastic deformation imposed during machining [30]. This study was performed by using coupons from

the rolling direction since the particular structural area under fatigue evaluation (aircraft skin) is loaded along the rolled direction of the material (also consistent with past research performed by DST Group on notched and un-notched AA7075-T6 coupon [28, 29]). However, if other aircraft structural points are to be examined, where fatigue life may be influenced by plastic anisotropy, coupons from both the rolling and long/short transverse directions should be obtained and tested.

The geometry of the of the strain-controlled coupon was in accordance with the ASTM E606/E606M standard [31], while the stress-controlled coupons were in accordance with the ASTM E466-07 standard [32].

2.1.1 Symmetric strain-controlled tests

Two strain-controlled tests were performed, at 1.5% and 1.8% strain for 65 and 100 cycles respectively [Fig. 1(a) and (b)]. In both cases, a relatively small amount of cyclic hardening is observed.

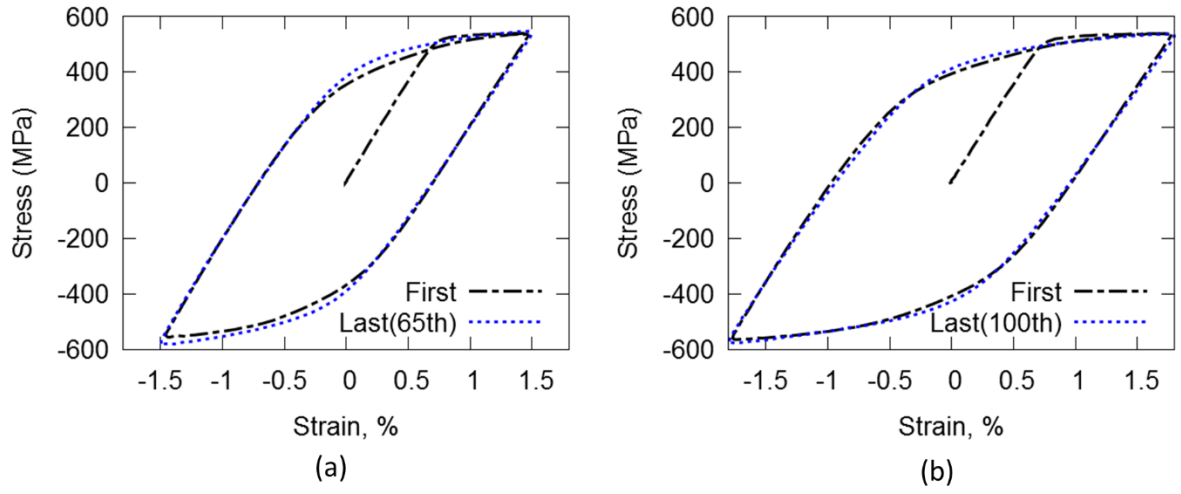

Figure 1 AA 7075-T6 symmetric strain-controlled test results: hysteresis loop at (a) 1.5% (1st and 65th cycles) and (b) 1.8% (1st and 100th) strain level.

2.1.2 Asymmetric strain-controlled tests

The load cases investigated include a combination of low and high strain amplitudes in order to assess a broad range of mean stress relaxation rates (Table 1). A total of 150 loading cycles have been performed in each test case.

Table 1 Asymmetric strain-controlled load cases

Test	$\varepsilon_{\min}$ (%)	$\varepsilon_{\max}$ (%)	ε_a (%)	ε_{m} (%)
1	-0.15	1.15	0.65	0.50
2	0.20	1.60	0.70	0.90
3	-0.05	1.55	0.80	0.75
4	0.05	1.65	0.80	0.85
5	0.15	1.45	0.65	0.80
6	-0.10	1.90	1.00	0.90

In Table 1, $\varepsilon_{\min}$ denotes the minimum strain, $\varepsilon_{\max}$ the maximum strain imposed during cycling, ε_a the strain amplitude, given by: $\varepsilon_a = \left(|\varepsilon_{\min}| - |\varepsilon_{\max}|\right)/2$, and ε_{m} the mean strain, given by $\varepsilon_m = \left(|\varepsilon_{\max}| + |\varepsilon_{\min}|\right)/2$.

The corresponding mean stress relaxation curves are shown in Fig. 2, where increasing strain amplitude results in faster mean stress relaxation. Only one case (Test 6) relaxes completely, while other load cases relax at large mean stresses, a phenomenon noticed in other materials [9, 12, 33].

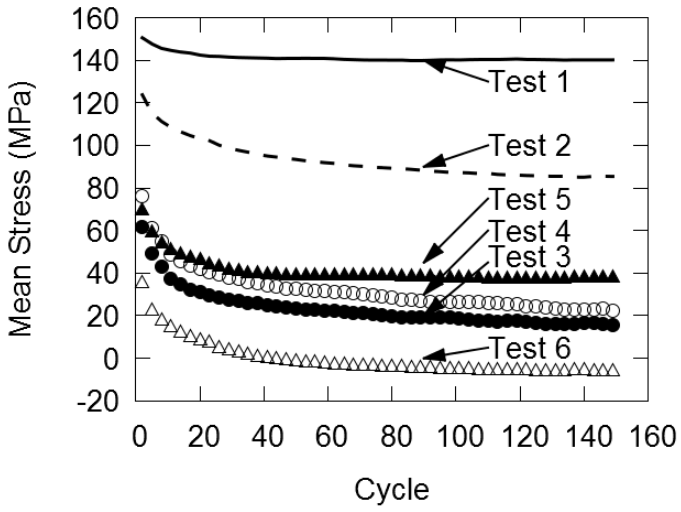

Figure 2 AA 7075-T6 mean stress relaxation curves for the asymmetric stain-controlled test cases (presented in Table 1).

The hysteresis loop development of Test 2 and Test 4 (both presented in Table 1) are more closely investigated in Fig. 3, where the first and last (150^{th}) cycle for each load case is compared. In both test cases, strain hardening is observed, as evidenced by the narrowing of the hysteresis loop. The narrow hysteresis loops in Test 2 [Fig. 3(a)] than in Test 4 [Fig. 3(b)] provide an indication of the varying amount of plastic deformation, with Test 4 inducing significantly more plastic deformation than Test 2.

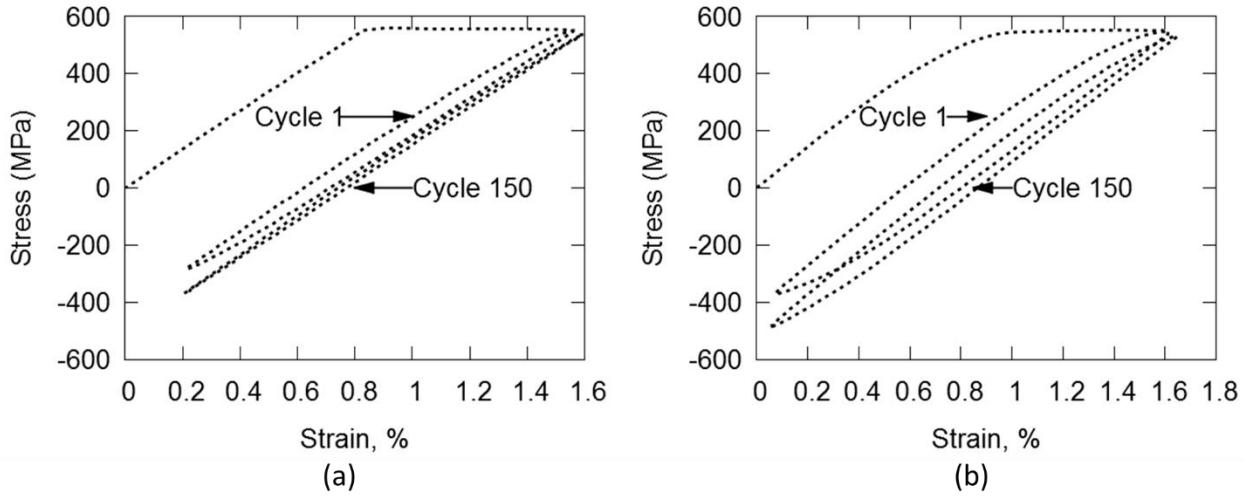

Figure 3 AA7075-T6 hysteresis loops obtained from the asymmetric strain-controlled (a) Test 2 (b) Test 4 (presented in Table 1). Comparison of the first and last (150th) cycle.

2.1.3 Asymmetric stress-controlled tests

The strain ratcheting behaviour of the material was investigated through a series of load cases (Table 2), which enabled the collection of a variety of ratcheting rates.

Table 2 Asymmetric stress-controlled load cases

Test	$\sigma_{\min}$ (MPa)	$\sigma_{\max}$ (MPa)	σ_a (MPa)	σ_{m} (MPa)
1	-430	510	470	40
2	-440	520	480	40
3	-460	540	500	40
4	-450	550	500	50

In Table 2, $\sigma_{\min}$ is the minimum strain, $\sigma_{\max}$ the maximum strain imposed during cycling, σ_a the strain amplitude, given by: $\sigma_a = \left(|\sigma_{\max}| - |\sigma_{\min}|\right)/2$), and σ_{m} the mean strain, given by $\sigma_m = \left(|\sigma_{\max}| + |\sigma_{\min}|\right)/2$.

The strain ratcheting curves obtained from the Table 2 tests cases are presented in Fig. 4, where two different calculation methods are used:

- Maximum strain $\varepsilon_{\max}$, at the peak of each cycle [Fig. 4(a)];
- Mean strain ε_m for each cycle (where: $\varepsilon_m = \left(|\varepsilon_{\max}| + |\varepsilon_{\min}|\right)/2$) [Fig. 4(b)].

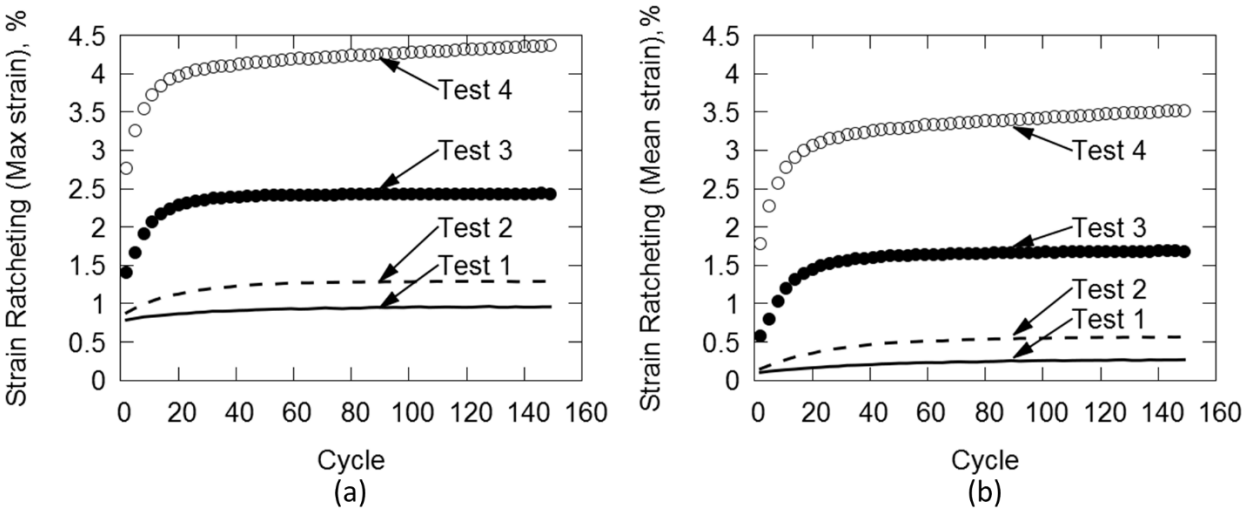

Figure 4 AA7075-T6 strain ratcheting curves for asymmetric-stress controlled tests (presented in Table 2): (a) maximum strain $\varepsilon_{\max}$, at peak, of each cycle (b) mean strain ε_m at each cycle.

An early onset of plastic shakedown (stabilisation of the plastic strain accumulation per cycle) can be observed in the Fig. 4 results, as evidenced by the saturation of ratcheting strain after approximately 20 cycles, which is an important phenomenon to consider in fatigue design [34]. A closer inspection of the hysteresis loop development for Test 2, Test 3 and Test 4 (Table 2) is provided in Fig. 5. In particular, the plastic shakedown is evidenced by the proximity (pile-up) of the hysteresis loops between cycle 20 and 100. Moreover, strain hardening for all test cases is identified as the progressive decrease in the hysteresis loop size between cycle 1 and 100.

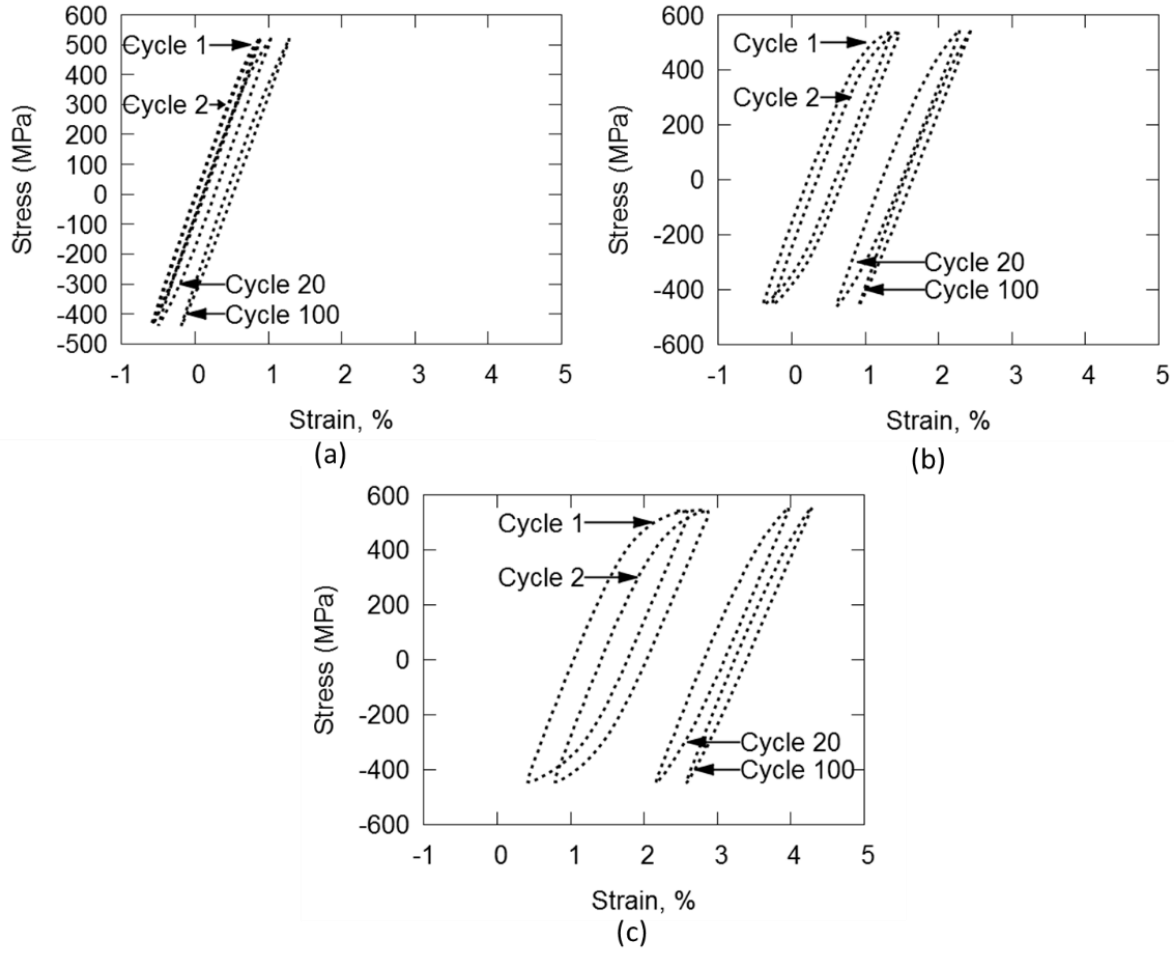

Figure 5 AA7075-T6 Hysteresis loops obtained from the asymmetric stress-controlled (a) Test 2 (b) Test 3 and (c) Test 4 (presented in Table 2). Comparison of the first and last (150th) cycle.

2.2 Cyclic Plasticity Modelling

2.2.1 Model Formulation

The nonlinear kinematic hardening model used in the sensitivity analysis was the Multicomponent Armstrong-Frederick (MAF) model, commonly referred in the literature as the Chaboche model [35]. Kinematic hardening implies the translation of the yield surface in the stress space, as described by the movement of the yield surface centre. The Chaboche material model enjoys a

very wide acceptance within the applied engineering and research community, mainly due to its simplicity, robustness and the fact that it is already embedded within commercial finite element (FE) analysis software. The Chaboche model has been the subject of many modifications aiming to improve the simulation ability of transient cyclic effects, such as mean stress relaxation and ratcheting, e.g. [36-41]. These modifications, offering enhanced simulation capabilities in the Chaboche model, are also able to improve fatigue results [12]. In the present study, the basic Chaboche model is selected as the test-bed for the strain-life fatigue sensitivity analysis.

Moreover, isotropic hardening was also included in the Chaboche model, so as to capture the cyclic hardening present in 7-series aerospace aluminium alloys [42]. Isotropic hardening implies the uniform expansion or contraction of the yield surface in the stress space, as described by the increase or the decrease of the yield surface radius. The isotropic hardening model chosen was the one proposed by Chaboche in [35], as it has been widely used in the past to model the hardening effect in various metallic materials.

The formulation of the complete cyclic plasticity model is presented in its uniaxial form, since the simulations are limited in the uniaxial stress space.

The yield surface applied was the Von Mises yield surface (f) given by Eq. 1:

$$f = (\sigma - X)^2 - R^2 \tag{1}$$

Where σ is the applied stress, X the back stress and R the yield stress evolving through the isotropic hardening rule [35] described by Eq. 2.

$$dR = b(R_s - R)\left|d\varepsilon^p\right| \tag{2}$$

where R_s is the saturating value of yield surface expansion and b gives the rate at which saturation is reached.

The total back stress X (controlling the yield surface shifting) is given by Eq. 3.

$$X = \sum_{i=1}^{3} X_i \tag{3}$$

The X_i back stress terms are obtained from Eq. 4 (d denotes the differential of each term).

$$dX_i = \begin{cases} \gamma_i \left(a_i d\varepsilon^p - X_i dp \right) & i = 1,2 \\ a_i d\varepsilon^p & i = 3 \end{cases} \tag{4}$$

where $d\varepsilon^p$, dp, a_i and γ_i are the incremental plastic strain, the equivalent plastic strain, the saturation level and rate of saturation respectively. Three back stress terms are defined as originally suggested by Chaboche [35], which is the minimum number needed to accurately simulate the cyclic behaviour. Moreover, selection of the minimum number of back stress terms was aimed at reducing computational times and ensuring ease of application of the model in the fatigue calculation software.

2.2.2 Determination of the model baseline parameters

The Chaboche model (kinematic and isotropic hardening) was implemented numerically using an implicit integration scheme. The kinematic hardening (back stresses X_i) parameters of the model were calculated by fitting Eq. 5 to the stabilised cyclic stress-strain curve (Fig. 6), according to the methodology proposed by Chaboche [35].

$$\frac{\Delta\sigma}{2} = \sigma_{yield} + \sum_{i=1}^{2} a_i \tanh\left(\gamma_i \frac{\Delta\varepsilon^p}{2}\right) + a_3 \frac{\Delta\varepsilon^p}{2} + R \tag{5}$$

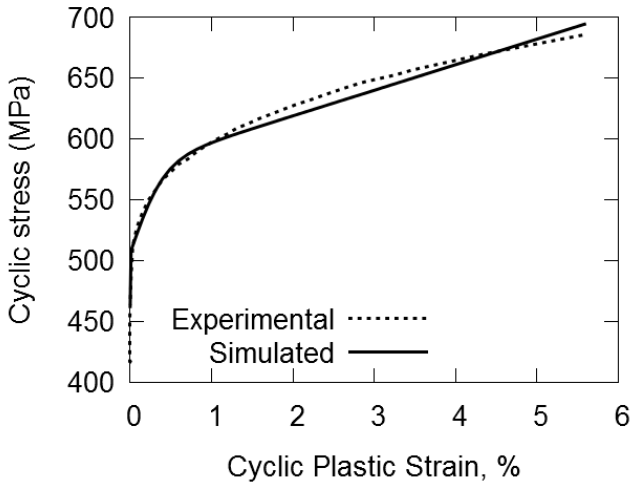

Figure 6 Curve fitting of the AA 7075-T6 experimental [43] and simulated stabilised cyclic stress-strain curve .

The isotropic hardening (R) parameters R_s and b were determined by nonlinear regression analysis to obtain the best fit to the cyclic stress range versus cycles data, with data collected from fully symmetric strain-controlled tests (Fig. 7) [9].

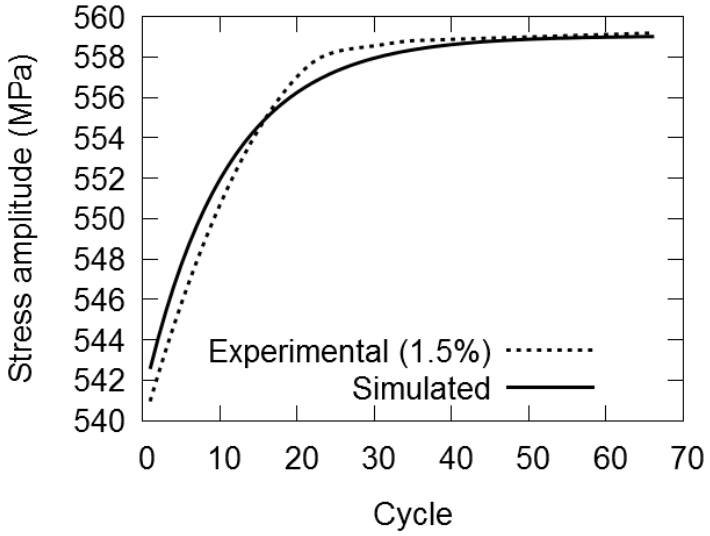

Figure 7 Simulated isotropic hardening compared against 1.5% symmetric strain controlled stress amplitude.

This technique was utilised to obtain the model baseline parameter values (shown in Table 3) that also acted as the range within which optimisation was performed (described in the sequel).

Table 3 Model baseline parameters

Elasticity Modulus	E = 69 GPa	
Cyclic yield stress	σ_{yield} = 465 MPa	
Kinematic hardening:		
X_1	a_1 = 41 MPa	γ_1 = 35,304
X_2	a_2 = 71 MPa	γ_2 = 242
X_3	a_3 = 2,100 MPa	N/A
Isotropic hardening:		
R	R_s = 15 MPa	
	b = 6.8	

3. Single Objective Optimisation

A single objective optimisation was conducted using the commercial optimisation software package modeFRONTIER [44]. The objective of the optimisation was to minimise the difference between the simulated stress-strain curves and experimental data. The process involves an initial population development based on a select range for each of the plasticity model parameters. These values are then fed in the plasticity model, implemented numerically using an implicit integration scheme, to simulate the defined load cases (hysteresis loop shape, strain ratcheting curves, etc.). The success of the trailed parameters in the generation are determined by comparing the simulation outputs with experimental data with the use of an objective function. Based on the objective function scores, the next generation evolves by employing an optimisation algorithm, which in this study is the genetic algorithm (GA). In this study the applied optimisation structure is referred to as a workflow. The sensitivity analysis required the development of a variety of workflows, where the main difference exists in the experimental curve definition and the imposed constraints. Varying the workflow definition allowed for the development of a number of parameter sets to be tested in strain-life fatigue predictions. In particular, the most suitable experimental curves are selected for the determination of those Chaboche model parameters, in terms of achieving better strain-life fatigue predictions. The overall optimisation process flow diagram is illustrated in Fig. 8, with its elements (objective function, constraints, etc.) described in detail in the following sections.

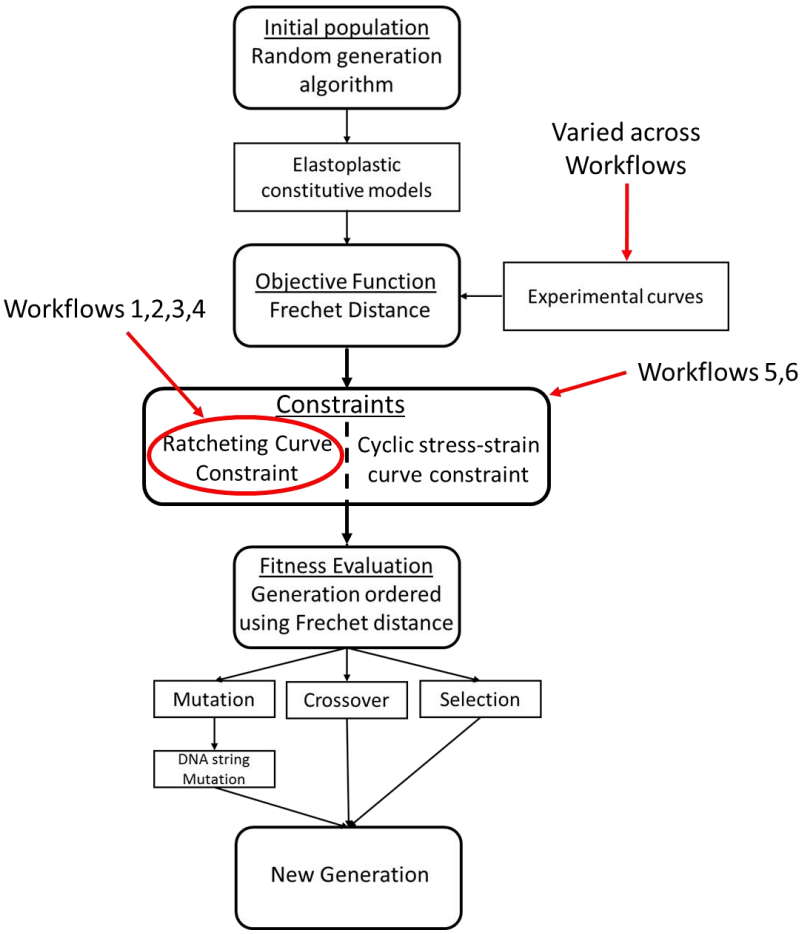

Figure 8 Overall optimisation process flow diagram

3.1 Population range

The range over which the population was developed is provided in Table 4, which includes the ranges for all workflows (1 to 6) used in the optimisation process.

Table 4 Parameter value selection range for each optimisation scheme (Search Workflow)

Parameter	Search Workflow	
	1 and 2	**3 to 6**
σ_{yield} (MPa)	(250, 500)	
a_1 and a_2 (MPa)	(1, 300)	
a_3 (MPa)	(1, 100000)	
γ_1 and γ_2	(1, 100000)	
R_s (MPa)	15	(50, 200)
b	6.8	(0.001, 100)
E (GPa)	69	(60, 75)

The minimum and maximum values selected for the ranges were based on the parameter values given in Table 3, which were obtained by applying the manual calculation parameter technique as demonstrated in [35, 45]. The large range selected for the genetic algorithm was to balance between search flexibility and convergence in solution.

3.2 Optimiser

A GA was utilised in the search for the most suitable combination of the parameters. In particular, the Multi-Objective Genetic Algorithm (MOGA-II) [44] was implemented. MOGA-II is an improved version of the MOGA, originally proposed by Poloni [46], utilising a smart multi search elitism and a set of operators (selection, classical one-point crossover, directional crossover and bit flip mutation). In order to customise and to improve the efficiency of MOGA-II for the elastoplastic constitutive model application, an extensive investigation into the probability of invocation of each operator was conducted. As with classical MOGA, MOGA-II represents each parameter as a binary string onto which one of the operators (predefined by the operator probability) is applied during the reproduction process. The MOGA-II algorithm is summarised as following:

MOGA-II Pseudo Code

1. *Generate initial random population (P) of size N and Elite set E*
2. *Evaluate objective values*
3. *Rank and sort based on the objective values (Pareto dominance)*
4. *Generate offspring population by the reproduction*
   - *4.1. Combine both population and elite sets $Q = P \cup E$*
   - *4.2. While Q>P, resize Q by randomly removing individuals*
   - *4.3. Based upon probability of invocation, randomly assign one operator (local tournament selection, directional crossover, one-point crossover or bit flip mutation) to compute the evolution from Q to R*
   - *4.4. Evaluate objective values of population R*
   - *4.5. Rank and sort based on the objective values (Pareto dominance)*
   - *4.6. Extract the elite individuals*
     - *4.6.1. Copy all non-dominated individuals of R to E and sort*
     - *4.6.2. Update E by eliminating the duplicates and the dominated individuals*
     - *4.6.3. While E>N, resize E by randomly removing the individuals*
5. *Until termination, go to Step 4 with R as a new P*

Each of the algorithm processes (selection, crossover and mutation) are described in the following sections.

3.2.1 Selection

Selection of the most elite individuals (those forming next generation without gene alteration) from the population is determined as those with the best fitness values based on the value normalised with respect to the generation's total fitness value. When investigating the influence of selection probability on convergence one can obtain the varying convergence curves for the tested probabilities (Fig. 9). All probabilities converge to the same objective value, with only the convergence speed varying between selection probabilities. The shape of the convergence curves suggests that if a high selection probability is used, then too many individuals are passed through to the next generation unmodified resulting in inefficient optimal gene evolution. However, if the selection probability is too small, too many good performing individuals are lost through gene alteration (crossover and mutation).

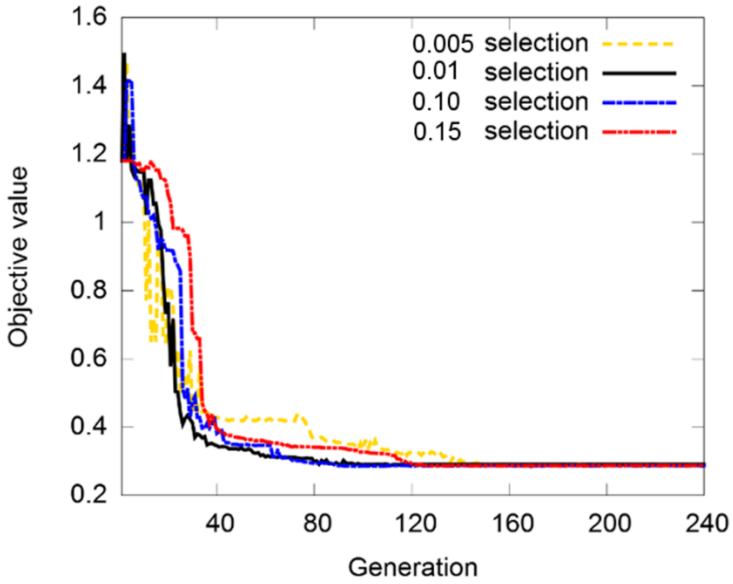

Figure 9 Convergence curve (Objective value variation vs generations) comparison when altering the selection probability values.

3.2.2 Crossover

One-point crossover is the most classical recombination operator, whereby two parents are chosen and some portion of the genetic material is exchanged between the parent variables vectors as illustrated in Fig. 10. The point of the crossover is randomly selected and all data beyond that point in either binary string is swapped between the two parents.

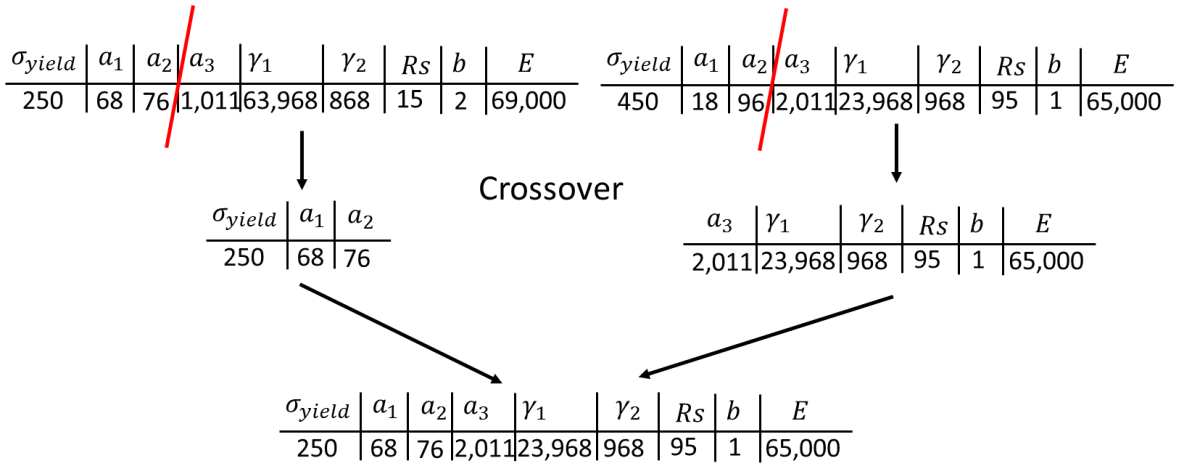

Figure 10 Crossover of genes in two parameter sets

Directional crossover is slightly different and assumes that a direction of improvement can be detected by comparing the fitness values of two reference individuals. Fig. 11 shows the influence of crossover probabilities on convergence. The larger crossover probabilities of 0.70 and 0.80 yield noisier results compared to the lower crossover probabilities of 0.40 and 0.50. This behaviour can be explained by considering how the extra crossover of genes can lead to a greater chance of carrying across of mutated genes to the next generation which are not as successful in simulation accuracy. Interestingly, the lowest crossover probability of 0.30 did not improve either the convergence rate or the converged objective value (compared to the 0.40 convergence curve). This suggests that if the crossover probability is too low, important genes, which could lead to improved simulation results, may be neglected too often, leading to an inability to reach the optimal convergence. Thus, the fastest and most successful convergence is obtained using lower probabilities of 0.40 and 0.50.

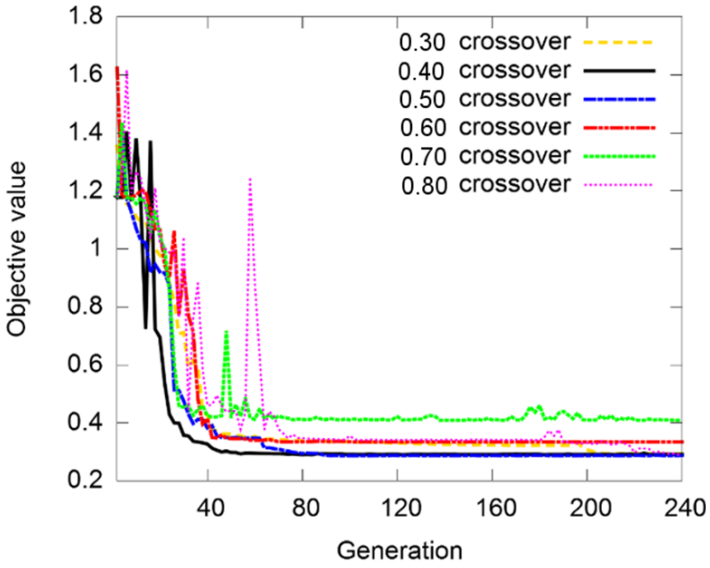

Figure 11 Convergence curve (Objective value variation vs generations) comparison when altering crossover probability.

3.2.3 Mutation

Mutation is an operator that ensures diversity from one generation to the next by introducing random changes in the genes of the individuals. This concept is shown in Fig. 12, where the binary converted gene is mutated. In MOGA-II it is possible to set DNA String Mutation Ratio, which dictates the amount by which each binary string is mutated, as demonstrated in Fig. 12, where 10% mutation ratio of an 80 string parameter set results in the mutation of 8 strings.

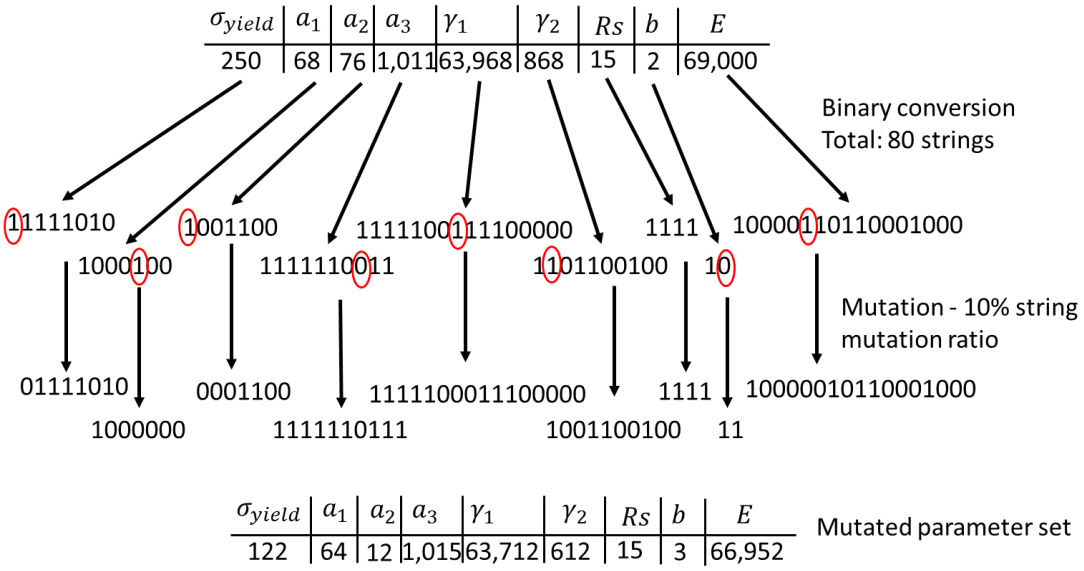

Figure 12 Mutation of a parameter set to produce a new individual to test in the next generation.

The curves in Fig. 13 (a) demonstrate a changing rate at which convergence is reached, as well as a changing convergence value between the tested mutation probabilities. The lower mutation probabilities converge prematurely but are significantly less noisy compared to the higher mutation probability curves. The reduced amount of mutation resulted in an inability of the optimiser to find a more suitable local optimal. The initial population has greater influence on the converging generation due to the lower influence of mutated genes. The optimisation outputs using mutation probabilities of 0.1 to 0.15 converge to the same objective value at approximately the same rate. The 0.05 mutation probability optimisation also converges to the same objective value but requires significantly more generations to achieve that. The convergence curve corresponding to the 0.1 mutation probability had the fastest convergence rate. Furthermore, the influence of DNA selection ratio on convergence is presented in Fig. 13 (b), which provides a comparison of the convergence

curves. The results illustrate that the lower ratio of 0.01 mutation resulted in the less successful convergence value, which suggested that if too little of the DNA string is mutated, it is more difficult for the optimisation process to find the optimal location in the population of parameter combinations. The ratios of 0.03, 0.05 and 0.1 resulted in the same converged objective value, with the main difference being in the convergence rate. The 0.1 mutation had the less successful convergence rate, while 0.03 and 0.05 had very similar convergence rates. Consequently, values ranging between 0.03 and 0.05 would provide the optimal convergence.

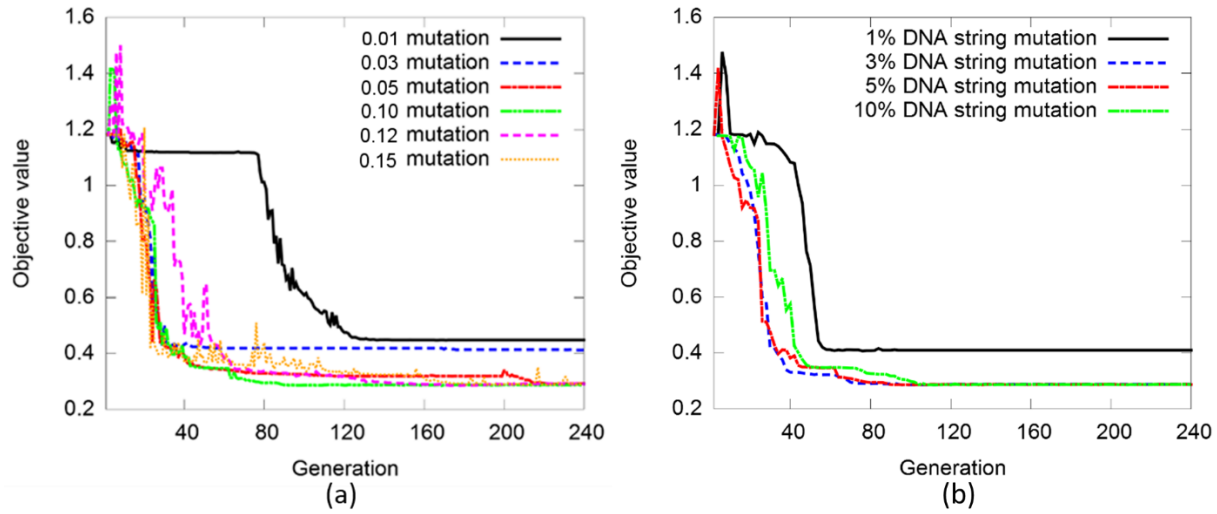

Figure 13 Convergence curve (Objective value variation vs generations) comparison when altering (a) mutation probability (b) DNA string mutation ratio.

3.2.4 Initial Population

The great influence of the initial population on the convergence of heuristic types of searches is well recognised [47, 48]. Therefore, to maximise the chances of finding optimal solutions, selecting the diversity and the optimal population size is very important. The curves in Fig. 14(a)

provide an indication of the influence of generation size on convergence. An initial generation size of 25 is considerably more time efficient and converges to a lower objective than the other tested generation sizes. Different initial population sequence generator algorithms were investigated in order to maximise the diversity. In particular, a comparison between the random sequence generator, Sobol sequence, Uniform Latin Hypercube (ULH) and Incremental Space Filler (ISF) was performed [Fig. 14(b)]. These results suggest that the Sobol initial population exhibits significantly faster convergence rates compared to the other sequence generators.

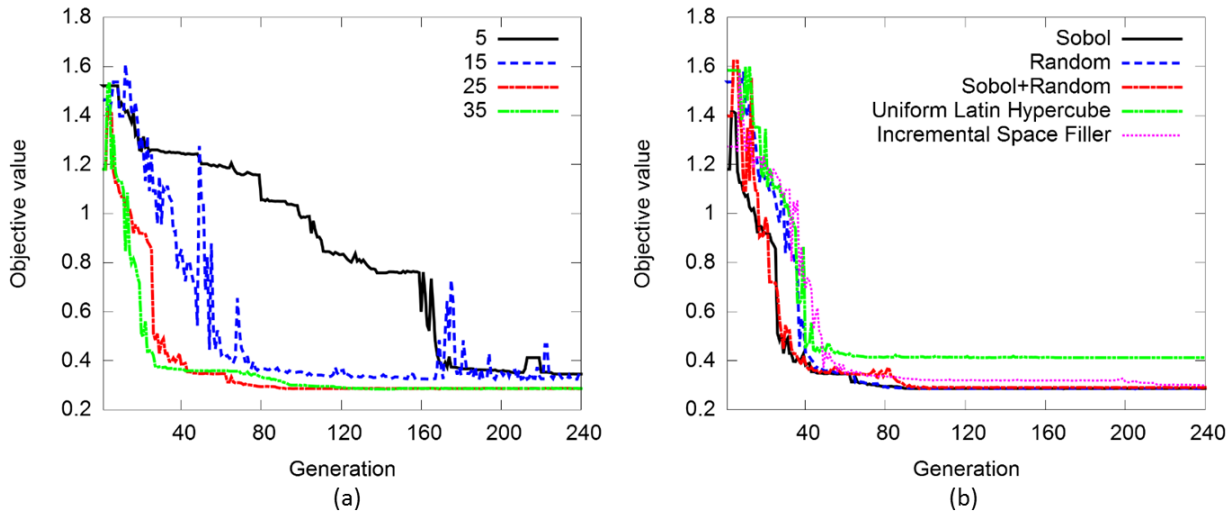

Figure 14 Convergence curve (Objective value variation vs generations) comparison when altering (a) generation size (b) initial population sequence generator algorithms.

3.2.5 Finalised optimiser

Based on this investigation, the GA settings for the elastoplastic constitutive model optimisation are listed in Table 5 and these were the values used in the optimiser for all workflows.

Table 5 Genetic Algorithm (GA) optimal parameters

Population		Selection Probability	Crossover Probability	Mutation	
Size	**Algorithm**			**Probability**	**DNA string mutation ratio**
25	Sobol	0.01	0.4	0.1	0.03

3.3 Objective function

The population of parameter combinations were fed into the model simulation stage, during which the parameters were used to generate the simulation outputs. The simulation outputs were then compared with experimental data and a fitness value was given by the objective function. The fitness value was defined according to the Frechet distance [49] which attempts to minimise the maximum Euclidean distance of possible ways to traverse the experimental curve and the simulated curve as summarised in Eq. 6, where the Frechet distance (FD) is calculated by comparing the functions of the curves P and Q (described in the MOGA-II Pseudo Code presented in section 3.2), where i and j in Eq. 6 corresponding to points defining the curve.

$$FD[i,j] = \max\left[\left\|P(i) - \mathrm{Q(j)}\right\|, \min\left(FD[i-1,j-1], \mathrm{FD}[i,j-1], \mathrm{FD}[i-1,j]\right)\right] \quad (6)$$

3.4 Constraints

It was important to ensure the gene development of the optimisation were not based on unrealistic simulation results. In some tested parameters, the results produced were deemed acceptable with regard to their fitness value but in fact produced unrealistic simulation results (e.g. prediction of decreasing ratcheting strain). Consequently, although the objective error was reduced, the actual appearance of the simulations curves were counterintuitive. To overcome this issue, constraints

were added to the optimisation to prevent the emergence of unrealistic solutions. This ensured that genes associated with unrealistic results were not used in further chromosome development in future generations. For that purpose, constraints were imposed on the ratcheting outputs. In particular, negative gradients occurring between strain outputs were restricted, as indicated in the regions defined by dashed lines in Fig. 15. This avoided the appearance of potential unrealistic outputs, such as the curve anomalies shown in red lines in Fig. 15.

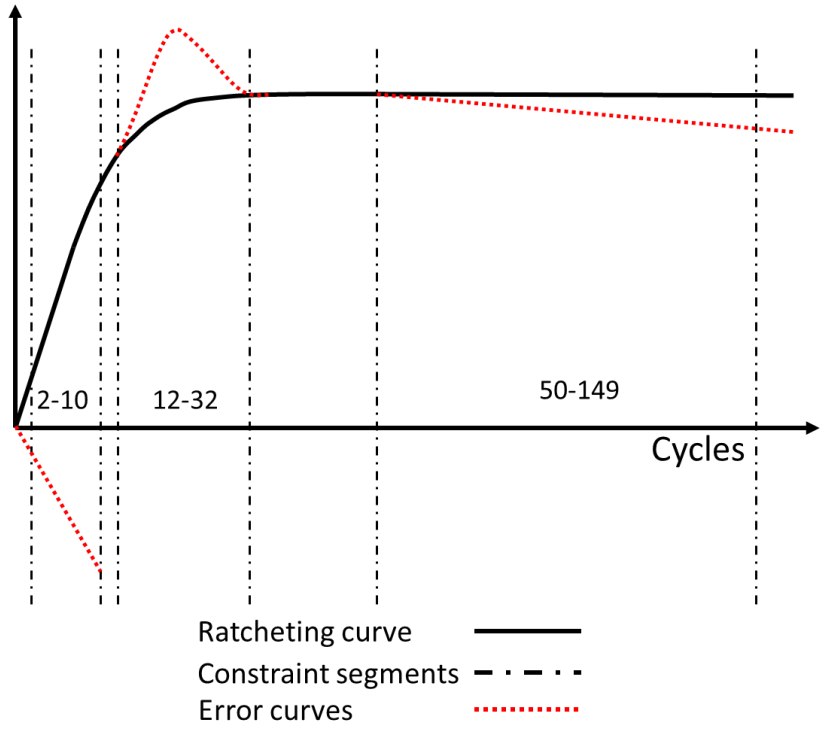

Figure 15 Ratcheting curve example (strain at peak of each loading cycle versus number of cycle): Dashed line segments define the constraint regions of the ratcheting output; dotted lines provide examples of what the constraints are attempting to prevent.

3.5 Search Workflows

The workflow used in the optimisation strategy has a significant influence on the development of the parameters. It is possible that a number of alternate parameter combinations can achieve the same uniaxial simulation results. So, it is important to determine what influence these different optimised parameter sets have on the strain-life fatigue prediction accuracy. In order to determine this, a sensitivity analysis was conducted where a number of different workflows were used in the parameter optimisation. These varying workflows are summarised in Table 6, which provides an overview of how the experimental definition of the workflows varied across the six tested versions (detailed description is included in the sections 3.5.1 to 3.5.6).

Workflow	**Strain controlled loading cases**				**Stress controlled asymmetric loading cases**			
	symmetric		**asymmetric**					
	+/-1.8%	**Various strain levels**	**(1.6,0.2)%**	**(1.65,0.05)%**	**(550,-450)**	**(540,-460)**	**(520,-440)**	**(510,-430)**
1	Stabilised hysteresis loop Shape				Maximum strain at Ratcheting Curve	Maximum strain at Ratcheting Curve		
2	Stabilised hysteresis loop Shape						Maximum strain at Ratcheting Curve	Maximum strain at Ratcheting Curve
3	Stabilised hysteresis loop Shape	Cyclic stress-strain curve	Stabilised hysteresis loop shape at cycle 1 and 100	Stabilised hysteresis loop shape at cycle 1 and 100				
				Mean stress relaxation curve				
4	Stabilised hysteresis loop Shape	Cyclic stress-strain curve			Mean strain at Ratcheting Curve	Mean strain at Ratcheting Curve		
					Hysteresis loop shape at cycle 1	Hysteresis loop shape at cycle 1, 2, 20 and 100		
5	Stabilised hysteresis loop Shape	Cyclic stress-strain curve			Mean strain at Ratcheting Curve	Mean strain at Ratcheting Curve		
		$\frac{\Delta\sigma_{cyclic}}{\Delta\varepsilon_{cyclic}^{plastic}} < 343MPa$			Hysteresis loop shape at cycle 1	Hysteresis loop shape at cycle 1, 2, 20 and 100		
6	Stabilised hysteresis loop shape	Cyclic stress-strain curve			Mean strain at Ratcheting Curve	Mean strain at Ratcheting Curve	Mean strain at Ratcheting Curve	
		$\frac{\Delta\sigma_{cyclic}}{\Delta\varepsilon_{cyclic}^{plastic}} < 343MPa$			Hysteresis loop shape at cycle 1	Hysteresis loop shape at cycle 1, 2, 20 and 100	Hysteresis loop shape at cycle 1	

Table 6 Summary of varying experimental curves used in each workflow

3.5.1 Workflow 1 and 2

The hysteresis loop shape and ratcheting strain simulation accuracy are important features to be used in the model parameter identification. Consequently, the experimental data used in the objective were:

Workflow 1:

- The stabilised 1.8% symmetric strain controlled hysteresis loop shown in Fig. 1(b).
- The two higher ratcheting strain curves labelled as Test 3 and Test 4 in Fig. 4(a).

Workflow 2:

- The stabilised 1.8% symmetric strain-controlled hysteresis loop shown in Fig. 1(b).
- The lower ratcheting strain curves labelled as Test 1 and Test 2 in Fig. 4(a).

The isotropic hardening parameters were not included in the optimisation process. Instead, as proposed in [9], they were determined by nonlinear regression analysis to obtain the best fit to the cyclic stress range versus cycles data gathered from fully symmetric strain controlled tests.

The convergence curves obtained from the two workflow strategies are compared in Fig. 16, which is developed from the most elite (lowest objective value) of the generation.

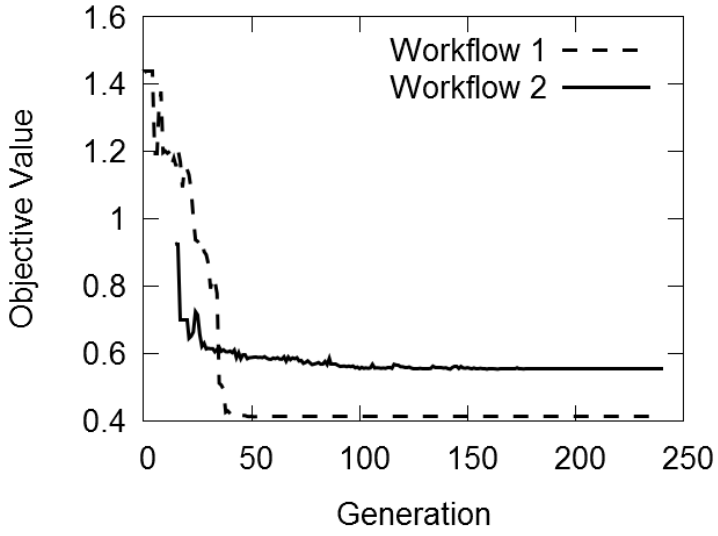

Figure 16 Convergence curves (objective value versus number of generations) obtained from workflows 1 and 2.

3.5.2 Workflow 3

It was deemed necessary to also consider parameter development based on the accurate simulation of the evolution of the hysteresis loop shape. Due to the complexity of the loading in the tested spectra it was important to predict the maximum and minimum stress and strains present at each point in the spectrum. Therefore, a balance between the progression of the back-stress, as well as the yield and isotropic hardening had to be developed. In this workflow, the isotropic hardening parameters were allowed to fluctuate to allow better flexibility. This feature offered enhanced opportunity to recognise the progressive change in the hysteresis loop shape which was noticeable in the experimental data. The experimental data used in the objective were:

- The stabilised 1.8% symmetric strain controlled hysteresis loop [shown in Fig. 1(b)].
- The first and 100th cycle of the asymmetric strain-controlled Test 2 and Test 4 (Fig. 3).

- The mean stress relaxation curve obtained from Test 4, shown in Fig. 2
- The cyclic stress strain curve, shown in Fig. 6.

Simulation results revealed that it was important to include the 100th cycle in the optimisation process to facilitate accurate development of the noticeable cyclic hardening phenomenon present in the material, which can be attributed to the narrowing of the hysteresis loops with cycles. The mean stress relaxation in the experimental curve definition was considered necessary in order to ensure that the parameters developed are able to simulate the progressive downward shift of the hysteresis loops between the 1st and 100th cycle. Finally, the cyclic stress-strain curve was also added to capture a variety of stabilised cycles.

The convergence curve corresponding to the optimisation is provided in Fig. 17. A solution was achieved (converged) within 240 generations.

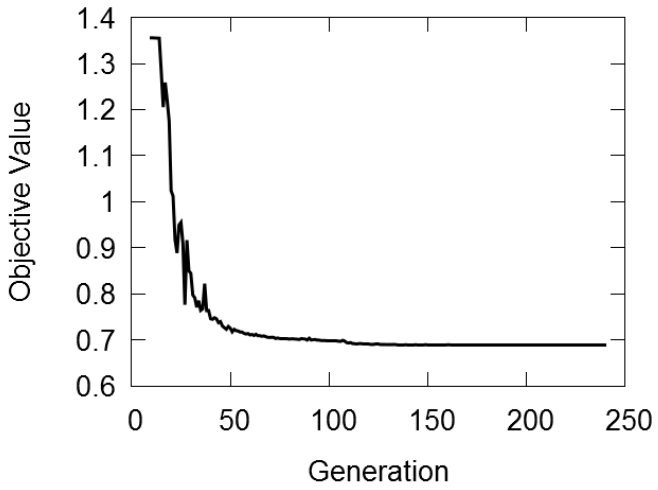

Figure 17 Convergence curve (objective value versus generations) from workflow 3 incorporating asymmetric strain-controlled hysteresis loop experimental curves.

3.5.3 Workflow 4

One key objective of this study was to determine whether the parameters developed from ratcheting hysteresis loops can provide improvement to strain-life fatigue calculations. The development of the hysteresis loops could be slightly different, leading to a different combination of kinematic and isotropic hardening parameters that may affect strain-life fatigue calculations. Due to the important influence of large overloads in the spectra, Workflow 4 was based on asymmetric stress-controlled data collected from large maximum stress load cases. Therefore, Workflow 4 included the following experimental curves:

- The stabilised 1.8% symmetric strain controlled hysteresis loop [shown in Fig. 1(b)].
- The asymmetric stress-controlled Test 3 and Test 4 strain ratcheting curves calculated by taking the mean strain ε_{m}, given by $\varepsilon_m = \left(\left|\varepsilon_{\max}\right| + \left|\varepsilon_{\min}\right|\right)/2$, which is shown in Fig. 4(b).
- The asymmetric stress-controlled Test 3 hysteresis loops at 1, 2, 20 and 100 cycles as per Fig. 5(b) and the first cycle from asymmetric stress-controlled Test 4, shown in Fig.5(c).
- The cyclic stress strain curve, shown in Fig. 6.

The inclusion of one cycle from the asymmetric stress controlled Test 4 was used to ensure the parameter search was not restricted to the development of a good fit for solely one load case, broadening the parameter search and robustness of the converged parameters. The convergence curve from Workflow 4 is provided in Fig. 18. The rate of convergence was relatively fast (objective value reached within 35 generations).

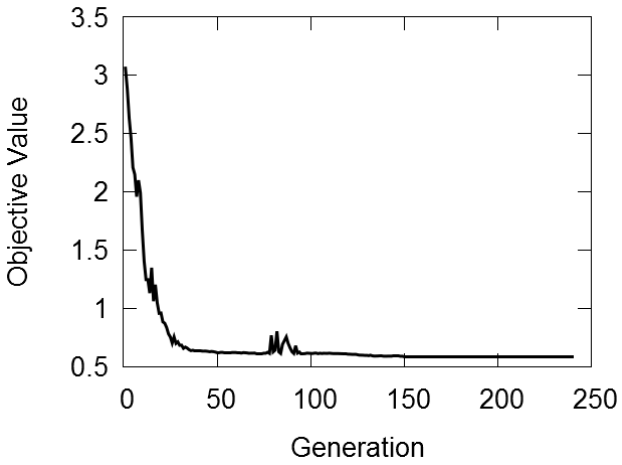

Figure 18 Convergence curve (objective value versus generations) obtained from workflow 4 which incorporates asymmetric stress-controlled experimental curves.

3.5.4 Workflow 5

Due to the large loads contained in the spectrum coupled with the notch factor, the predicted stress and strain has the potential to violate the experimental bounds of the cyclic stress-strain curve. Predicting stresses or strains outside the bounds of this curve would lead to inaccurate results caused by the large negative stress and strains resulting in inaccurate damage calculations. The produced inconsistency is illustrated in the Fig. 19 example, showing how fatigue life (in flight hours) calculated at one particular critical location counterintuitively increases with increasing notch intensity factor K_t. This is attributed to the prediction of an unrealistically large negative stress and strain, forcing subsequently developed hysteresis loops to predict no further damage accumulation.

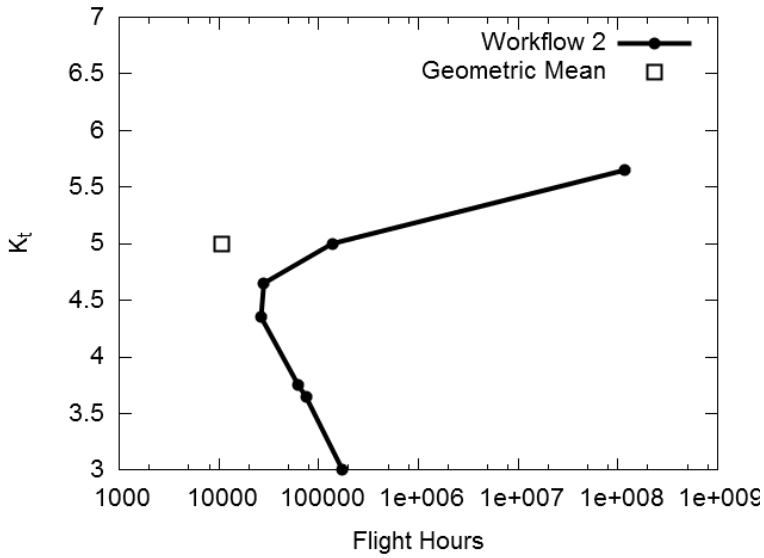

Figure 19 Fatigue (in flight hours) prediction with increasing notch intensity factor (K_t).

To mitigate this issue, a constraint was added to the workflow whereby the end of the predicted cyclic-stress strain curve was forced to saturate according to Eq. 7, as indicated by the red line in Fig. 20. This constraint ensures that stresses outside the bounds of the cyclic stress-strain curve were not being over-predicted.

$$\frac{\Delta\sigma_{cyclic}}{\Delta\varepsilon_{cyclic}^{plastic}} < 343MPa \tag{7}$$

In particular, the 343 MPa constraint corresponds to the (slope of the) limiting red-line curve shown in Fig. 20 and practically this curve is obtained through curve fitting. It is noted that the Fig. 20 (same as Fig. 6) curve is the cyclic stress - strain curve.

Workflow 5 had the same experimental curve definition as Workflow 4 (described in section 3.5.3), with the only difference being the aforementioned additional constraint on the simulation outputs based on the saturation of the cyclic stress-strain curve.

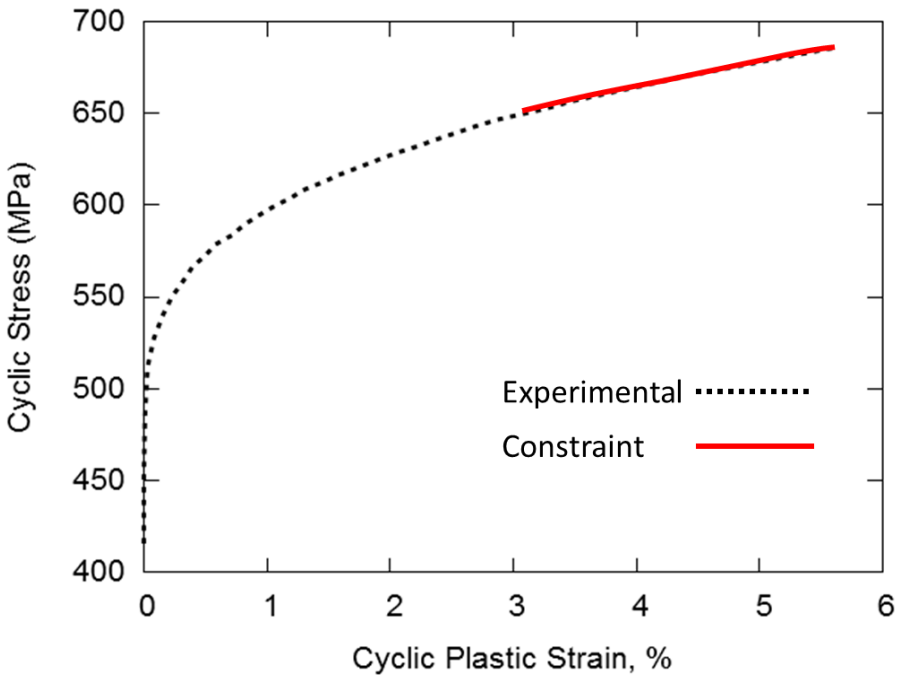

Figure 20 AA7075-T6 cyclic stress-strain curve with gradient constraint indicated by solid line (experimental curve obtained from [43])

The convergence curve obtained from Workflow 5 is shown in Fig. 21, which exhibits a very similar response as the other workflows employed in the optimisation (1 to 4).

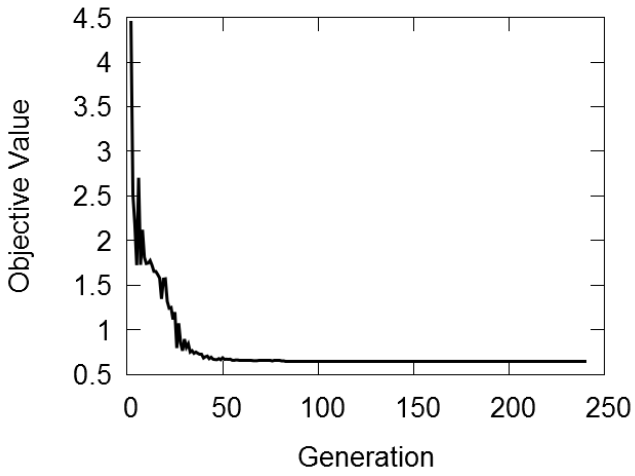

Figure 21 Convergence curve (objective value versus generations) obtained from the Workflow 5 which incorporates asymmetric stress-controlled experimental results and saturated cyclic stress-strain curve.

3.5.5 Workflow 6

In order to determine the influence of lower maximum stress load cases, such as asymmetric stress controlled Test 1 and Test 2, on the parameter development for strain-life fatigue, Workflow 6 included additional experimental curves based on a low maximum stress load case. In particular, this workflow included the following experimental curves:

- The stabilised 1.8% symmetric strain controlled hysteresis loop [shown in Fig. 1(b)].
- The asymmetric stress-controlled Test 2, Test 3 and Test 4 strain ratcheting curves calculated by taking the mean strain ε_{m}, given by $\varepsilon_m = \left(\left|\varepsilon_{\max}\right| + \left|\varepsilon_{\min}\right|\right)/2$, which is shown in Fig. 4(b).

- The asymmetric stress-controlled Test 3 hysteresis loops at 1, 2, 20 and 100 cycles as per Fig. 5(b) and the first cycle from asymmetric stress-controlled Test 2, shown in Fig.5(a) and Test 4, shown in Fig. 5(c).
- The cyclic stress strain curve, shown in Fig. 6.

The inclusion of experimental data collected from Test 2 enabled the parameter search to become broader in an attempt to find a set of parameters which can adequately recognise this variance in plastic behaviour between Test 2 and Test 4.

The objective value converged in approximately 50 generations, as demonstrated in Fig. 22.

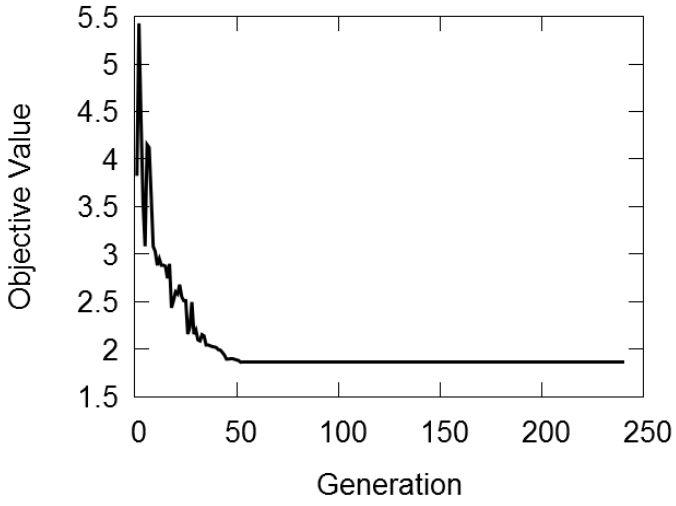

Figure 22 Convergence curve (objective value versus generations) obtained from Workflow 6 using large and low maximum stress asymmetric stress-controlled experimental data

4. Results

4.1 Output of optimisation process

The cyclic plasticity (Chaboche) model parameters obtained from the optimisation process, for each search workflows employed (1 to 6), are listed in Table 7. This set of parameters were then applied to perform the strain-life fatigue predictions, presented in section 4.2 of this paper.

Table 7 Optimised plasticity (Chaboche) model parameters for each search workflow

Parameter	Workflow					
	1	**2**	**3**	**4**	**5**	**6**
σ_{yield} (MPa)	368	441	112	357	221	309
a_1 (MPa)	68	100	187	172	167	183
a_2 (MPa)	76	21	163	300	170	68
a_3 (MPa)	1011	7375	4010	2122	102	102
γ_1	63,968	77	4,885	274	85,928	468
γ_2	889	99,982	62	1	168	59,779
R_s (MPa)	15	15	187	80	120	120.2
b	6.8	6.8	100	61	46	72
E (GPa)	69	69	67.3	73.2	69.8	62.2

4.2 Strain-life fatigue predictions

Predicted fatigue lives were compared against experimental data gathered as part of the 2010 P-3C Orion aircraft service life assessment program conducted at the Australian Defence Science and Technology (DST) Group [29]. The programme collected notched coupon fatigue data using spectra obtained from fatigue critical locations identified in both the Royal Australian Air Force (RAAF) and the United States Navy (USN) full scale fatigue tests. In the analysis conducted in this work, a total of 21 spectra and corresponding experimental fatigue data were compared against strain-life predictions calculated using the DST Group developed fatigue analysis program CGAP [50], which employs a fatigue-life tool FAMS [51]. The main components of the CGAP strain-life calculation process are summarised below:

- Neuber's rule is used to calculate the notch stress and strains using the remote loading condition.
- Equivalent strains are calculated using the strain-life curve and the modified Morrow equation [5].
- The total fatigue damage is calculated using the Miner's rule [52].

The fatigue predictions using the six workflows were compared to the predictions obtained using the Masing model [1]. This was performed by integrating the Chaboche model into the strain-life calculation process by replacing the Masing model, resulting in the Chaboche model being used to calculate the local stress and strains at the notch root. This comparison was performed to determine whether the parameters obtained by applying the objective combinations considered in the present study were able to improve the strain-life prediction of the existing CGAP-incorporated

model. This was performed by comparing the total accumulated error across the 21 different spectra, calculated using Eq. 8.

$$ERROR = \sum_{i=1}^{21} \left| \frac{EXP_i - SIM_i}{EXP_i} \right| \tag{8}$$

where EXP_i and SIM_i are correspondingly the experimental and simulated data point corresponding to spectrum i, with $i = 1, 2, 3, .., 21$.

An interesting finding is the anomalies produced by Workflows 2, 3, and 4, in terms of the obtained fatigue predictions. In particular, Fig. 23 demonstrates these issues, with respect to the results obtained from one large load spectrum. What is noticeable from at the areas enclosed by the dashed lines in Fig. 23, is the increase of the predicted fatigue lives (flight hours) with the increase in the notch intensity factors K_t. This is counterintuitive, indicating an issue with the calculation of the stress and strain as the loading increases. Therefore, on the basis of the resulting anomalies, the corresponding workflows (2, 3 and 4) were disqualified.

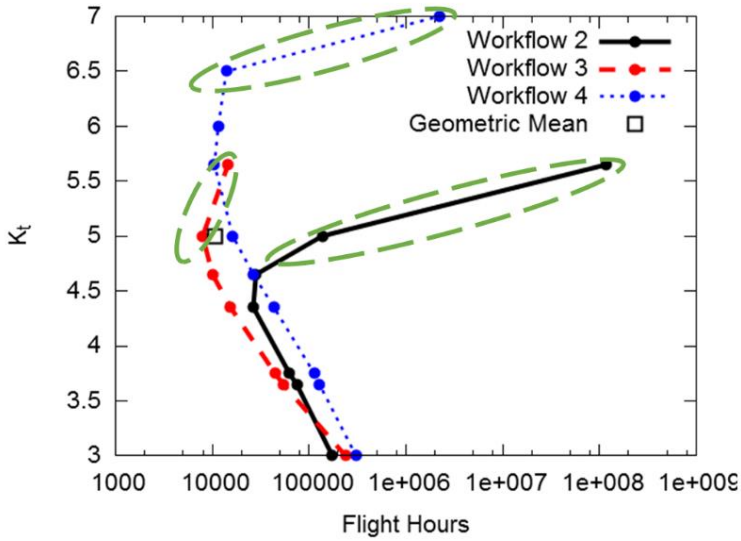

Figure 23 Fatigue prediction anomalies produced using a large load spectrum

The predicted lives for the three workflows (1, 5 and 6) capable of successfully predicting the fatigue life for all spectra (i.e., without results containing anomalies) are presented in Fig. 24. The corresponding total accumulated error for each workflow is also shown in this figure. As indicated by the error value, Workflow 5 provides better overall improvement (16.41%) in life prediction among all workflows. This is also evidenced by the number of points concentrated closer to the diagonal (one-to-one line). Interestingly, Workflow 6, which is largely based on Workflow 5, resulted in significantly worse life predictions compared to the other two workflows (1 and 6) and the Masing model predictions.

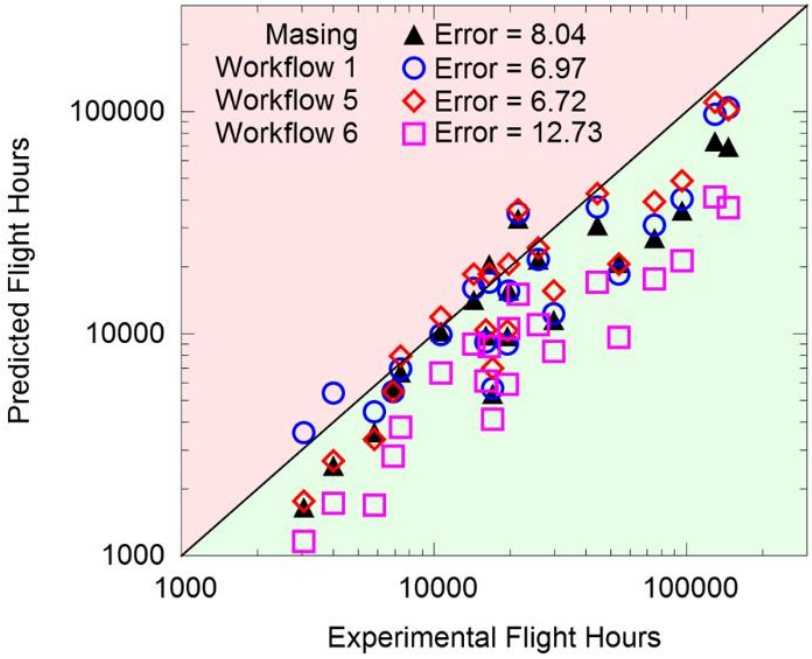

Figure 24 Optimisation workflow fatigue predictions plotted against the corresponding geometric mean of the experimental results.

In order to provide a better understanding on the accuracy achieved in each spectrum, the difference between experimental and predicted fatigue life was calculated with the use of Eq. 9.

$$ERROR_i = \frac{|EXP_i - SIM_i|}{EXP_i} \tag{9}$$

where $ERROR_i$, EXP_i and SIM_i are correspondingly the error, experimental data and simulated data point corresponding to each spectrum i, with $i = 1, 2, 3, .., 21$.

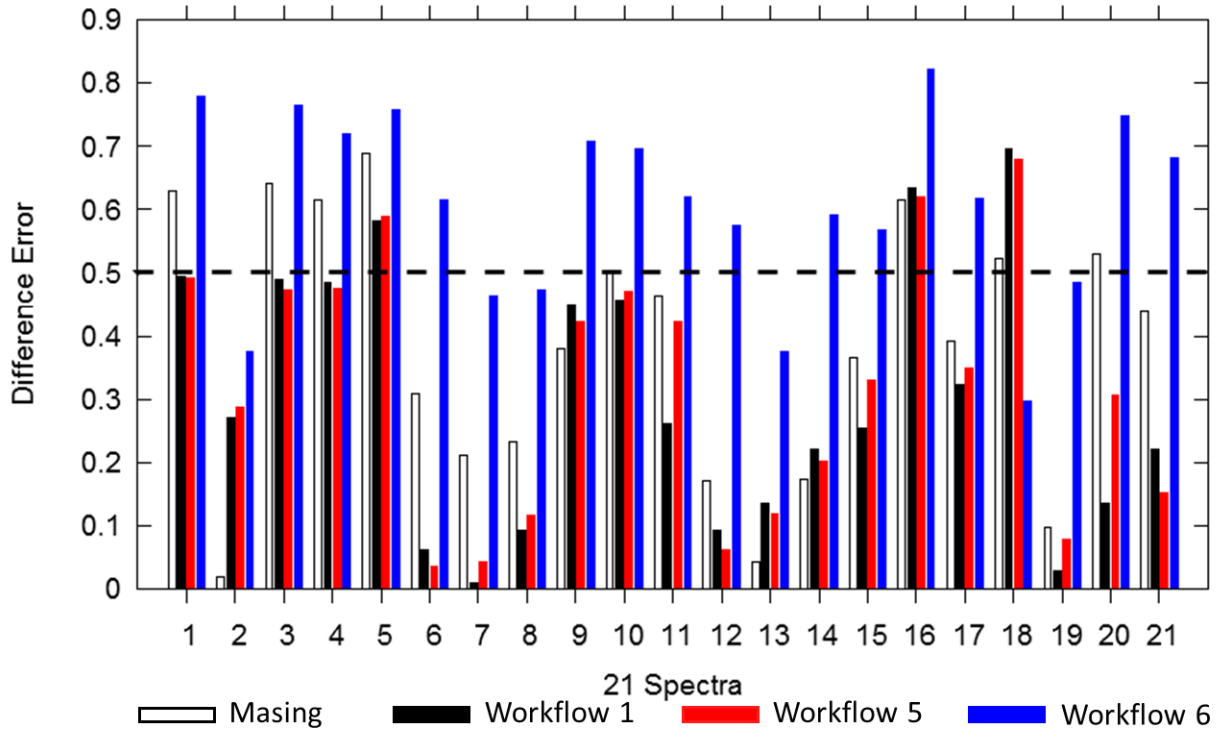

Figure 25 Difference in predicted and geometric mean for each of the 21 tested spectra

The results obtained for all 21 load spectra are plotted in Fig. 25. In all cases, Workflow 6 does not provide any improvement on the prediction. The two ratcheting based workflows (Workflow 1 and 5) demonstrate significant improvement compared to Masing. Considering the line drawn at 50% error, both Workflow 1 and 5 decreased the number of predicted lives exceeding 50% error from 8 to 3.

5. Discussion

The critical analysis of the Chaboche model parameter determination has demonstrated the level of influence that the type of uniaxial material data has on the accuracy of the strain-life fatigue predictions. This finding is not merely new, from a research point of view, however in light of the extensive use of the Chaboche model in actual fatigue life calculations, it is an issue that should be highlighted to the engineering practitioners employing this model on design and structural integrity management applications. Moreover, an interesting new finding is related to parameter determination with the use of asymmetric strain-controlled uniaxial data. This kind of data have caused anomalies in the prediction of the fatigue lives for the case of large notch intensity factors. This anomaly was the consequence of the imbalance between yield stress and kinematic hardening. In particular, if the yield stress is too low, then an increased number of loads in the spectrum will produce plastic stress and strain. This offers an explanation as to why increasing the size of the loads in the spectrum would likely cause a decrease in fatigue life.

The accuracy improvement achieved with the use of Workflow 1 provides some evidence on the importance of developing parameters according to asymmetric stress-controlled data. However, as discussed, Workflow 4 fatigue predictions contradicts this finding, as life prediction increases with the increase of notch intensity factor. This anomaly can be attributed to the inclusion of the cyclic stress strain curve, since in some spectra the maximum stress was greater than the bounds of the cyclic stress-strain curve. Due to the small gradient at the end of the curve (having a slight positive value), the prediction of stresses outside of the bounds were constantly increasing in magnitude. Constraining these stresses to saturate outside the bounds, as was the case in Workflows 5 and 6, prevented the occurrence of the counterintuitive results. This resulted in Workflow 5 having the

most accurate predictions, as evidenced by the total accumulated error and the 50% error improvement.

Although Workflow 2 highlighted the importance of considering only the larger maximum stress load cases in the model parameter determination, workflow 6 tested this further with the inclusion of low maximum stress experimental curves (in addition to those already defined in Workflow 5). The inclusion of the lower maximum stress load case resulted in a significant decrease in fatigue prediction accuracy, with reference to the accumulated error and Fig. 24 and Fig. 25 presented results. Comparing the developed parameters from Workflow 5 and 6 (shown in Table 7) it is apparent that the most significant difference is in the size of the yield stress. Workflow 6 employs a much larger yield stress to improve the simulation accuracy in the low maximum stress load case. Consequently, compressive loading in the spectrum may not produce any compressive plastic strain, which leads effectively to accumulation of (tensile) plastic strain. This is effect is highlighted in Fig. 26 (extracted hysteresis loops from a tested spectrum), which demonstrates how plastic strain accumulation obtained through Workflow 6 leads to higher damage when compared with Workflow 5. An over-calculation in damage estimation leads to lower predicted fatigue lives, as it has been demonstrated for Workflow 6 (Fig. 24). The lower yield stress in Workflow 5 results in more compressive plastic strain, reducing the tensile plastic strain stacking noticed in Workflow 6 (clustering of hysteresis loops at lower plastic strain illustrated in Fig. 26).

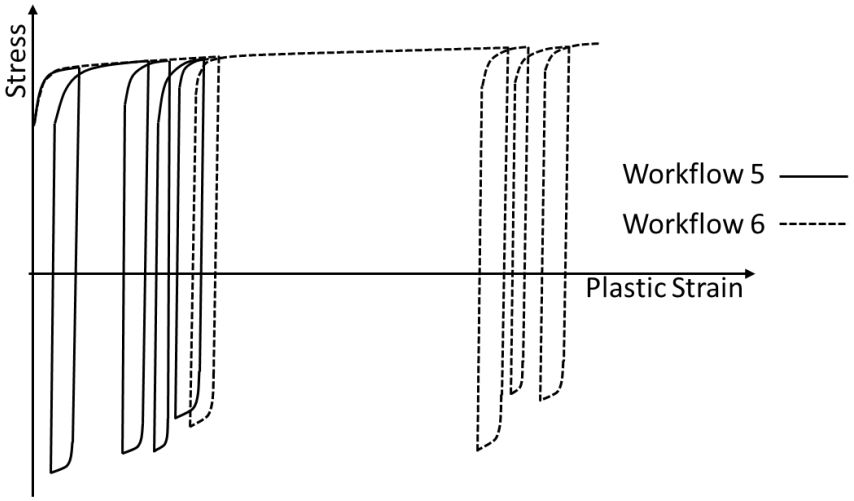

Figure 26 Extracted hysteresis loops from a tested spectrum, indicating the difference between Workflow 5 and Workflow 6 calculation.

The slight improvement in Workflow 5, in comparison to Workflow 1, can be explained by referring to the values of the added back stresses (a_i) and the saturation level obtained for the calculated stress. In particular, the saturation level for Workflow 5 is higher than that of workflow 1. This was due to the inclusion of the cyclic stress-strain curve in Workflow 5. Consequently, for the tested spectra, the predicted mean stresses in Workflow 1 can be lower than the one predicted by Workflow 5, which effectively reduces the influence on fatigue life. Moreover, Workflow 1 uses a higher yield stress than that of Workflow 5, which is a consequence of not including in the workflow the asymmetric stress-controlled hysteresis loop shape data. This causes the same issues as highlighted in Workflow 6 (illustrated in Fig. 26). The influence of the larger plastic strain accumulation is slightly negated by the lower predicted mean stress, since the larger plastic strain accumulation will decrease the predicted life, while the lower tensile means stresses will raise the predicted life. Therefore, Workflow 5 provides the most accurate combination of both plastic strain and mean stress simulation.

Based on the results of this study, the optimal uniaxial material data to be used in the development of the elastoplastic constitutive model parameters for strain-life fatigue predictions is based on large maximum stress asymmetric stress-controlled hysteresis loops [load cases capable of inducing significant plastic strains as those given in Fig. 5(b) and 5(c)] and their corresponding strain ratcheting curve. For completeness, the cyclic stress-strain curve should also be included with a constraint to saturate outside the bounds of the curve, developed from known experimental data.

Conventional methods of parameter development as outlined by Chaboche[35] use stabilised hysteresis loops from symmetric strain-controlled results and/or the cyclic stress-strain curve to develop an initial set of parameters. These parameter values are then altered by fitting cyclic transient data from obtained from a large number of load cases. From the point of view of the effort required for this exercise, this is especially important when the Chaboche model is applied for strain-life fatigue analysis involving complex loading histories, such as those included in aircraft load spectra.

The conducted analysis showed that the Chaboche model parameter optimisation exercise can be more efficient when targeted to those experimental data (both symmetric and asymmetric stress/strain controlled) that can be the most influential in capturing successfully the transient effects. In particular, it was found that the material data can be narrowed down to the following:

- The cyclic stress-strain curve;
- The symmetric stain-controlled stabilised hysteresis loop, at one or two strain levels;

- The hysteresis loop development of at least two stress-controlled load cases inducing a large amount of plastic strain (e.g. 3-5% for aluminium alloys) and their corresponding ratcheting curves (plastic strain accumulation versus cycles).

In summary, this study showed that:

- The use of the Chaboche model parameters obtained from the optimisation process, has improved significantly the fatigue predictions, when compared to the CGAP-embedded Masing model predictions.
- The sensitivity analysis has showed that, using appropriately selected uniaxial material (test) data, improved strain-life fatigue predictions can be achieved, as opposed to randomly selected or too extensive test data.

6. Conclusion

The Chaboche nonlinear kinematic hardening model has been used successfully in a sensitivity analysis intended to determine the importance of the experimental curves' type and constraints used in elastoplastic constitutive model parameter development for strain-life fatigue predictions. The application of an optimisation strategy using optimal GA settings, allowed for greater parameter search capabilities leading to a number of different parameter sets. The sensitivity of the strain-life calculation based on these different parameter sets was used to determine which material data provided the most accurate strain-life fatigue results, therefore, providing a better understanding into the importance of the type of material data used in plasticity model parameter determination. Based on these results, an optimisation strategy using optimal generic algorithm has been successfully developed to identify multiple model parameters that yield significantly

improved prediction than conventional method. This study has also highlighted the importance of accurately simulating the hysteresis loop sequences. Stress and strains calculated early in the spectrum sequence are expected to have a significant influence on the overall damage calculation, due to their contribution to the size of future stress and strain later in the spectrum.

In future research work, the validity of this devised method will be tested on other aerospace alloys (aluminium and titanium), for fatigue predictions of spectra obtained from other aircraft fatigue critical locations (e.g. a number of control points of P-3C aircraft fatigue management programme). Moreover, it is noted that due to funding constraints the test campaign was focused on obtaining results from a broad spectrum of load cases, rather than limiting the cases and re-running experiments to check repeatability. Thus, further research efforts are planned to include repeat test runs of the symmetric strain, asymmetric strain and asymmetric stress-controlled loading cases conducted in this study.

Acknowledgements

The financial support of the Defence Science and Technology Group (DSTG) of the Australian Department of Defence (DSTO-RMIT Research Agreement ref. 2014/1032188/1) is acknowledged. The authors would also like to thank Dr Xiaobo Yu of DSTG for his valued guidance.

References

[1] G. Masing, "Self stretching and hardening for brass (in German)," in *Second International Congress for Applied Mechanics*, Zurich, Switzerland, 1926, pp. 332-335.

[2] Z. Xia, D. Kujawski, and F. Ellyin, "Effect of mean stress and ratcheting strain on fatigue life of steel," *International Journal of Fatigue*, vol. 18, pp. 335-341, 7// 1996.

[3] Y. Jiang and P. Kurath, "An Investigation of Cyclic Transient Behavior and Implications on Fatigue Life Estimates," *Journal of Engineering Materials and Technology*, vol. 119, pp. 161-170, 1997.

[4] C. Bleuzen, M. Chaudonneret, L. Farcy, J. Flavenot, and N. Ranganathan, "Fatigue testing and life prediction for notched specimens of 2024 and 7010 alloys subjected to aeronautical spectra," presented at the Amzallag (Ed.), Automation in Fatigue and Fracture: Testing and Analysis, Philadelphia, 1994.

[5] N. E. Dowling, "Mean stress effects in strain–life fatigue," *Fatigue & Fracture of Engineering Materials & Structures*, vol. 32, pp. 1004-1019, 2009.

[6] N. E. Dowling, A. Arcari, C. A. Calhoun, and D. C. Moore, "Strain-based fatigue for high-strength aluminum alloys," in *Annual Forum Proceedings - AHS International*, 2009, pp. 2718-2729.

[7] A. Arcari, R. De Vita, and N. E. Dowling, "Mean stress relaxation during cyclic straining of high strength aluminum alloys," *International Journal of Fatigue*, vol. 31, pp. 1742-1750, 2009.

[8] H. Hao, D. Ye, Y. Chen, M. Feng, and J. Liu, "A study on the mean stress relaxation behavior of 2124-T851 aluminum alloy during low-cycle fatigue at different strain ratios," *Materials and Design*, vol. 67, pp. 272-279, 2015.

[9] W. Hu, C. H. Wang, and S. Barter, "Analysis of Cyclic Mean Stress Relaxation and Strain Ratchetting Behaviour of Aluminium 7050," Defence Science and Technology Organisation, Melbourne, 1999.

[10] K. A. Zakaria, S. Abdullah, and M. J. Ghazali, "Comparative study of fatigue life behaviour of AA6061 and AA7075 alloys under spectrum loadings," *Materials and Design*, vol. 49, pp. 48-57, 2013.

[11] A. Arcari, "Enhanced strain-based fatigue methodolgy," Doctor of Philosophy in Engineering Mechanics, Virginia Polytechnic Institute and State University, Blacksburg, VA, 2010.

[12] J. L. Chaboche, P. Kanouté, and F. Azzouz, "Cyclic inelastic constitutive equations and their impact on the fatigue life predictions," *International Journal of Plasticity*, vol. 35, pp. 44-66, 8// 2012.

[13] Y. Jiang, W. Ott, C. Baum, M. Vormwald, and H. Nowack, "Fatigue life predictions by integrating EVICD fatigue damage model and an advanced cyclic plasticity theory," *International Journal of Plasticity*, vol. 25, pp. 780-801, 2009.

[14] W. P. Hu and C. Wallbrink, "Fatigue life analysis of specimens subjected to infrequent severe loading using a nonlinear kinematic hardening cyclic plasticity model," presented at the Advanced Materials Research, 2014.

[15] J. S. Novak, D. Benasciutti, F. De Bona, A. Stanojević, A. De Luca, and Y. Raffaglio, "Estimation of material parameters in nonlinear hardening plasticity models and strain life

curves for CuAg alloy," in *1st International Conference on Materials, Processing and Product Engineering 2015, MPPE 2015*, 2016.

[16] E. Khademi, G. H. Majzoobi, N. Bonora, and D. Gentile, "Experimental modeling of strain-dependent cyclic plasticity for prediction of hysteresis curve," *Journal of Strain Analysis for Engineering Design*, vol. 50, pp. 314-324, 2015.

[17] M. Cermak, R. Halama, T. Karasek, and J. Rojicek, "Parameter identification of chaboche material model using indantation test data and inverse approach," in *COUPLED PROBLEMS 2015 - Proceedings of the 6th International Conference on Coupled Problems in Science and Engineering*, 2015, pp. 743-752.

[18] A. H. Mahmoudi, H. Badnava, and S. M. Pezeshki-Najafabadi, "An application of Chaboche model to predict uniaxial and multiaxial ratcheting," in *Procedia Engineering*, 2011, pp. 1924-1929.

[19] K. M. Zhao and J. K. Lee, "Finite element analysis of the three-point bending of sheet metals," *Journal of Materials Processing Technology*, vol. 122, pp. 6-11, 2002.

[20] N. Khutia and P. P. Dey, "Material parameter optimisation of Ohno-Wang kinematic hardening model using multi objective genetic algorithm," *International Journal of Computational Materials Science and Surface Engineering*, vol. 6, pp. 50-74, 2014.

[21] M. Franulović, R. Basan, and I. Prebil, "Genetic algorithm in material model parameters' identification for low-cycle fatigue," *Computational Materials Science*, vol. 45, pp. 505-510, 2009.

[22] G. H. Farrahi, A. Shamloo, M. Felfeli, and M. Azadi, "Numerical simulations of cyclic behaviors in light alloys under isothermal and thermo-mechanical fatigue loadings," *Materials and Design*, vol. 56, pp. 245-253, 2014.

[23] H. Badnava, S. M. Pezeshki, K. Fallah Nejad, and H. R. Farhoudi, "Determination of combined hardening material parameters under strain controlled cyclic loading by using the genetic algorithm method," *Journal of Mechanical Science and Technology*, vol. 26, pp. 3067-3072, 2012.

[24] S. M. Rahman, T. Hassan, and S. Ranji Ranjithan, "Automated parameter determination of advanced constitutive models," in *American Society of Mechanical Engineers, Pressure Vessels and Piping Division (Publication) PVP*, 2005, pp. 261-272.

[25] S. Sinaie, A. Heidarpour, and X. L. Zhao, "A multi-objective optimization approach to the parameter determination of constitutive plasticity models for the simulation of multi-phase load histories," *Computers and Structures*, vol. 138, pp. 112-132, 2014.

[26] G. J. Yun and S. Shang, "A self-optimizing inverse analysis method for estimation of cyclic elasto-plasticity model parameters," *International Journal of Plasticity*, vol. 27, pp. 576-595, 2011.

[27] A. H. Mahmoudi, S. M. Pezeshki-Najafabadi, and H. Badnava, "Parameter determination of Chaboche kinematic hardening model using a multi objective Genetic Algorithm," *Computational Materials Science*, vol. 50, pp. 1114-1122, 2011.

[28] D. Mongru, P. Jackson, K. Maxfield, and C. Wallbrink, "Evaluation of Alternative Life Assessment Approaches Using P-3 SLAP Test Results DSTO-TR-2418," Melbourne, Australia2010.

[29] E. Matricciani, J. Duthie, and K. Walker, "DST Group P-3 FAMS/FASTRAN Recalibration Coupon Testing in Support of the 2010 Structural Management Plan Review,

DST-Goup_TR-2659," Defence Science and Technology Group, Melbourne, Australia2016.

[30] J. S. Robinson and W. Redington, "The influence of alloy composition on residual stresses in heat treated aluminium alloys," *Materials Characterization*, vol. 105, pp. 47-55, 07// 2015.

[31] "ASTM E606/E606M-12, Standard Test Method for Strain-Controlled Fatigue Testing," ed. West Conshohocken, PA: ASTM International, 2012.

[32] "ASTM E466-07, Standard Practice for Conducting Force Controlled Constant Amplitude Axial Fatigue Tests of Metallic Materials," ed. West Conshohocken, PA: ASTM International, 2007.

[33] D. L. Wu, F. Z. Xuan, S. J. Guo, and P. Zhao, "Uniaxial mean stress relaxation of 9-12% Cr steel at high temperature: Experiments and viscoplastic constitutive modeling," *International Journal of Plasticity*, vol. 77, pp. 156-173, 2016.

[34] Y. Sun, S. L. Shen, X. H. Xia, and Z. L. Xu, "A numerical approach for predicting shakedown limit in ratcheting behavior of materials," *Materials and Design*, vol. 47, pp. 106-114, 2013.

[35] J. L. Chaboche, "Time Independent Constitutive Theories for Cyclic Plasticity," *International Journal of plasticity*, vol. 2, pp. 493-496, 1986.

[36] J. L. Chaboche, "On some modifications of kinematic hardening to improve the description of ratchetting effects," *International Journal of Plasticity*, vol. 7, pp. 661-678, // 1991.

[37] N. Ohno and J. D. Wang, "Kinematic hardening rules with critical state of dynamic recovery, part I: formulation and basic features for ratchetting behavior," *International Journal of Plasticity*, vol. 9, pp. 375-390, 1993.

[38] Y. Jiang and H. Sehitoglu, "Modeling of cyclic ratchetting plasticity, part I: Development of constitutive relations," *Journal of Applied Mechanics, Transactions ASME*, vol. 63, pp. 720-725, 1996.

[39] Y. F. Dafalias, K. I. Kourousis, and G. J. Saridis, "Multiplicative AF kinematic hardening in plasticity," *International Journal of Solids and Structures*, vol. 45, pp. 2861-2880, 5/15/ 2008.

[40] H. P. Feigenbaum, J. Dugdale, Y. F. Dafalias, K. I. Kourousis, and J. Plesek, "Multiaxial ratcheting with advanced kinematic and directional distortional hardening rules," *International Journal of Solids and Structures*, vol. 49, pp. 3063-3076, 11/1/ 2012.

[41] G. R. Ahmadzadeh and A. Varvani-Farahani, "Ratcheting assessment of materials based on the modified Armstrong-Frederick hardening rule at various uniaxial stress levels," *Fatigue and Fracture of Engineering Materials and Structures*, vol. 36, pp. 1232-1245, 2013.

[42] A. Arcari and N. E. Dowling, "Modeling mean stress relaxation in variable amplitude loading for 7075-T6511 and 7249-T76511 high strength aluminum alloys," *International Journal of Fatigue*, vol. 42, pp. 238-247, 9// 2012.

[43] I. J. Zatz and A. J. Davidson, "Summary of Material Constants for Current Grumman Strain-Cycling Fatigue Prediction Method," Grumman Aerospace Corporation1979.

[44] ESTECO, "ModeFrontier," ed. http://ww.esteco.com, 2015.

[45] S. Bari and T. Hassan, "Anatomy of coupled constitutive models for ratcheting simulation," *International journal of plasticity*, vol. 16, pp. 381-409, 2000.

[46] C. Poloni and V. Pediroda, "GA coupled with computationally expensive simulations: tools to improve efficiency," in *Genetic Algorithms and Evolution Strategy in Engineering and Computer Science*, ed Chichester, UK: John Wiley & Sons 1997, pp. 267-288.

[47] E. K. Burke, S. Gustafson, and G. Kendall, "Diversity in Genetic Programming: An Analysis of Measures and Correlation with Fitness," *IEEE Transactions on Evolutionary Computation*, vol. 8, pp. 47-62, 2004.

[48] E. Zitzler, K. Deb, and L. Thiele, "Comparison of multiobjective evolutionary algorithms: empirical results," *Evolutionary computation*, vol. 8, pp. 173-195, 2000.

[49] H. Alt and M. Godau, "Computing the Frechet Distance Between Two Polygonal Curves," *International Journal of Computational Geometry & Applications*, vol. 05, pp. 75-91, 1995.

[50] C. Wallbrink and W. Hu, "A Strain-Life Module for CGAP: Theory, User Guide and Examples," Defence Science and Technology Organisation, Melbourne2010.

[51] Naval Air Warefare Centre, "Fatigue Analysis of Metallic Structures (FAMS) - A Computer Program to Calculate Fatigue Damage by Local Stress/Strain Approach," 1995.

[52] M. A. Miner, "Cumulative damage in fatigue," *Journal of Applied Mechanics*, vol. 12, pp. A159-A164, 1945.